

Accuracy vs. Complexity for mmWave Ray-Tracing: A Full Stack Perspective

Mattia Lecci, *Student Member, IEEE*, Paolo Testolina, *Student Member, IEEE*,
Michele Polese, *Member, IEEE*, Marco Giordani, *Member, IEEE*,
Michele Zorzi, *Fellow, IEEE*

Abstract

The millimeter wave (mmWave) band will provide multi-gigabits-per-second connectivity in the radio access of future wireless systems. The high propagation loss in this portion of the spectrum calls for the deployment of large antenna arrays to compensate for the loss through high directional gain, thus introducing a spatial dimension in the channel model to accurately represent the performance of a mmWave network. In this perspective, ray-tracing can characterize the channel in terms of Multi Path Components (MPCs) to provide a highly accurate model, at the price of extreme computational complexity (e.g., for processing detailed environment information about the propagation), which limits the scalability of the simulations. In this paper, we present possible simplifications to improve the trade-off between accuracy and complexity in ray-tracing simulations at mmWaves by reducing the total number of MPCs. The effect of such simplifications is evaluated from a full-stack perspective through end-to-end simulations, testing different configuration parameters, propagation scenarios, and higher-layer protocol implementations. We then provide guidelines on the optimal degree of simplification, for

Mattia Lecci, Paolo Testolina, Marco Giordani, and Michele Zorzi are with the Department of Information Engineering, University of Padova, Padova, Italy (email: {name.surname}@dei.unipd.it). Michele Polese is with Institute for the Wireless Internet of Things, Northeastern University, Boston, MA, 02120 USA (email: m.polese@northeastern.edu).

This work was partially supported by NIST through Award No. 70NANB18H273. Mattia Lecci's and Paolo Testolina's activities were also supported by *Fondazione CaRiPaRo* under the grants "Dottorati di Ricerca" 2018 and 2019, respectively.

The identification of any commercial product or trade name does not imply endorsement or recommendation by the National Institute of Standards and Technology, nor is it intended to imply that the materials or equipment identified are necessarily the best available for the purpose.

A preliminary version of this paper that did not consider end-to-end performance evaluations was presented at the *IEEE Information Theory and Applications Workshop (ITA)*, February 2020 [1].

©2020 IEEE. Personal use of this material is permitted. Permission from IEEE must be obtained for all other uses, in any current or future media, including reprinting/republishing this material for advertising or promotional purposes, creating new collective works, for resale or redistribution to servers or lists, or reuse of any copyrighted component of this work in other works.

which it is possible to reduce the complexity of simulations with a minimal reduction in accuracy for different deployment scenarios.

I. INTRODUCTION

Recent developments have paved the way towards 5th generation (5G) cellular networks and enhanced Wireless Local Area Network (WLAN) designs, to address the traffic demands of the 2020 digital society [2]. In particular, 5G systems will support very high data rates (with a peak of 20 Gbps in ideal conditions), ultra-low latency (around 1 ms for ultra-reliable communications), and a 100x increase in energy efficiency with respect to previous wireless generations. To meet those requirements, the 3rd Generation Partnership Project (3GPP) has released a set of specifications for NR, the new 5G Radio Access Network (RAN), which include (i) a flexible frame structure, with adaptive numerologies, (ii) network slicing and virtualization in a new core network design, and (iii) communications in the millimeter wave (mmWave) bands [3]. Similarly, the Institute of Electrical and Electronics Engineers (IEEE) has developed amendments to 802.11 networks, namely 802.11ad and 802.11ay [4], which operate at mmWaves. 3GPP NR carrier frequency can be as high as 52.6 GHz for Release 15 (even though future Releases will not exclude extensions up to 71 GHz [5]), while IEEE 802.11ad and 802.11ay exploit the unlicensed spectrum at 60 GHz [4].

The vast amount of available spectrum at mmWave frequencies can enable multi-Gbps transmission rates [6]. Moreover, the very short wavelength makes it practical to build large antenna arrays (e.g., with hundreds of elements) and establish highly directional communications, thus boosting the network performance through beamforming and spatial diversity [7].

Despite these promising characteristics, propagation at mmWaves raises several challenges for the design and performance of the whole protocol stack [8]. First, the communication suffers from severe path loss (which is inversely proportional to the square of the wavelength), thereby preventing long-range omni-directional transmissions. Second, mmWave links are highly sensitive to blockage from common materials (e.g., brick and mortar), which may result in more than 40 dB of attenuation at 28 GHz when losing Line-of-Sight (LoS) [9]. Third, the delay and the Doppler spread (which determine the temporal and frequency selectivity of the channels) are particularly strong at these frequencies and may lead to network disconnections [10]. Finally, directional communications require the precise alignment of the transmitter and receiver beams, hence

implying an increased control overhead for channel estimation and mobility management [11], [12].

The combination of these phenomena makes the mmWave channel extremely volatile to mobile users. Although some early performance evaluations have suggested that mmWave networks can offer orders of magnitude greater capacity than legacy systems (e.g., [13]), a deeper understanding of the propagation channel is required to reliably characterize such networks. In this sense, experimental testbeds make it possible to examine the network performance in real-world environments with extreme accuracy [14]. However, the prohibitive cost and limited flexibility of these platforms make this approach impractical for most of the research community [15].

Therefore, theoretical analyses and computer-aided simulations have emerged as an important tool in evaluating the performance of novel solutions and the interplay between the mmWave channel and the deployment and protocol design. Both analysis and simulation, however, require proper modeling of signal propagation to accurately reproduce the behavior of mmWave systems [16], [17]. On one side, analytical studies model the channel using a Nakagami-m or Rayleigh distribution [18], [19], [20]. This approach, while simplifying the analysis significantly, assumes a rich multipath channel when in fact it is sparse at mmWaves [21]. Similarly, stochastic Spatial Channel Models (SCMs), e.g., [22] for 3GPP NR, characterize the channel as a combination of random variables fitted from real-world measurements, providing a more realistic assessment of the mmWave network performance compared to their analytical counterparts [23], however for measurements at sub-6 GHz. Still, the stochastic nature of these models may prevent researchers from evaluating the impact of the channel dynamics in specific environments, and may respond poorly to the need of accurately characterizing the spatio-temporal evolution of the channel Multi Path Components (MPCs) [24].

Conversely, Ray-Tracers (RTs) can be used to precisely model the propagation of mmWave signals in specific scenarios [25], [26]. Unlike analytical or stochastic models, RTs are based on the geometry of the scenario and characterize the different propagation properties of each MPC, including time delay, Doppler shift, polarization, Angle of Departure (AoD) at the Transmitter (TX), and Angle of Arrival (AoA) at the Receiver (RX), thus providing higher accuracy [27]. Moreover, simulators can use ray-tracing to model the temporal and spatial evolution of the channel, a necessary feature for a proper planning of wireless systems. However, the generation of the MPCs can be computationally expensive, limiting the scalability of simulations. It is thus fundamental to find a compromise between accuracy and reliability, a research challenge that,

to date, has not yet been exhaustively addressed in the literature.

This paper represents a first, comprehensive study on how simplifications to a mmWave RTs-based channel modeling can reduce the computational complexity of system-level simulations without compromising their accuracy. Specifically, we target the following objectives:

- We propose simplification techniques for ray-tracing based on the Method of Images (MoI) to speed up network simulations and the RT itself. Specifically, along the lines of our previous investigations [1], [24], we consider a simplified RT implementation that processes only MPCs whose received power is above a certain threshold (relative to the strongest MPC) and another that limits the maximum number of reflections for each MPC.
- We showcase a publicly available and open-source RT¹ supporting a Quasi Deterministic (QD) model (which combines deterministic channel components with random rays representing the diffusion due to the roughness of the surfaces on which the rays reflect), the aforementioned simplifications strategies, and all the scenarios shown in our results.
- As our main contribution, we carry out an extensive system-level simulation campaign to quantify the impact of the RT simplifications on several network metrics. Unlike in our previous contribution [1]:
 - We consider a full-stack performance evaluation and the impact of the simplifications on different simulators. To do so, we integrate the RT implementation in ns-3 [28], [29], a network simulator with a complete TCP/IP protocol stack that makes it possible to simulate the end-to-end network performance, and in a custom MATLAB simulator (as in [1]), for link-level metrics. Specifically, we characterize the Signal-to-Interference-plus-Noise Ratio (SINR), throughput, and latency for different traffic regimes at the application layer and different antenna architectures, as a function of the degree of simplifications that are introduced on the RT. We also consider both indoor and outdoor scenarios, to characterize different mobility and propagation characteristics, as well as different antenna array configurations. Additionally, with ns-3, we simulate the interaction of the simplifications with different transport layer protocols, namely User Datagram Protocol (UDP) and Transmission Control Protocol (TCP), and with different applications. Our results show that there exist some configurations for which the impact

¹<https://github.com/wigig-tools/qd-realization>

of the RT simplifications is limited, especially when higher-layer performance metrics are considered, with a reduction in simulation complexity of up to 4 times.

- We assess the effect of the QD model on the network performance. Notably, we show that the additional stochastic diffuse components make the throughput and latency fluctuate more over time, while the RT simplifications generally result in more stable channels.
- We provide guidelines on the optimal working points, corresponding to the best combination of simplifications and system configurations, for which it is possible to decrease the computation time and complexity of simulations with a minimal reduction in accuracy with respect to the baseline RT implementation (i.e., without simplifications).

The rest of this article is structured as follows. In Sec. II we review the most relevant analytical, stochastic, and deterministic models for the mmWave channel, while in Sec. III we present the QD model we adopted for ray-tracing operations at mmWaves. In Sec. IV we describe the proposed simplifications to be applied to the RT, while performance results are provided in Sec. V. Finally, Sec. VI concludes the paper with suggestions for future work.

II. CHANNEL MODELING AT MMWAVES

The modeling of the mmWave channel, in terms of propagation and fading, has been a key research topic in recent years [16]. Multiple measurement campaigns have tried to characterize the properties of different portions of the mmWave spectrum, in a variety of different scenarios and environments, e.g., urban [6], rural [30], and indoor [31], [27].

These campaigns have led to the definition of different channel models. Comprehensive reviews, discussing propagation, fading, and beamforming models can be found in [21], [32], while [33] focuses on the various results on propagation loss. These efforts have identified the key factors for an accurate modeling of the mmWave channel. First, multipath components are sparse in the angular domain, thus an accurate model should explicitly characterize the angle of arrival and departure of the different taps. Moreover, as discussed in Sec. I, blockage at the considered frequencies has a more remarkable impact on the link dynamics than at sub-6 GHz, which should be accounted for. Finally, rough surfaces could generate more diffuse scatterers than at longer wavelengths.

The aforementioned measurement campaigns have led to different modeling approaches for the mmWave channel, which have various degrees of complexity and accuracy, and can be applied

to different contexts and evaluations. In the next paragraphs, we will review three broad families, i.e., channel models used for mathematical analysis, stochastic, and map-based models.

Analytical Channel Models: Analytical studies for the coverage and capacity evaluation of mmWave networks generally considered simplified channel models, based on propagation and a single random variable for fading. Rayleigh and Nakagami- m fading models have been widely used in stochastic geometry analysis of mmWave systems, such as, for example, in [20], [18], [19]. Nakagami- m fading, introduced in [34], controls the amplitude of fading through the parameter m , so that it is possible to model differently the LoS and Non-Line-of-Sight (NLoS) fading phenomena. Similarly, Rayleigh fading is widely used, as in a stochastic geometry context it provides an easily tractable exponential form of the Nakagami fading for $m = 1$ [19]. Moreover, the Nakagami- m or Rayleigh fading is generally employed with a sectorized beamforming model for directional transmissions. This accounts for the beamforming gain G by assigning a maximum gain G_M to a main lobe, of angular width θ_b , and a lower gain G_m for the simplified side lobes in the complementary angular space [20]. This simplified model limits the accuracy in the representation of the interaction between the mmWave propagation, the realistic antenna arrays, and the beamforming strategies [16]. While only being relevant for omnidirectional, multipath-rich channels at sub-6 GHz, its tractability is desirable for analytical derivations even if it may not accurately model a realistic mmWave channel.

Stochastic Channel Models: An improved characterization can be achieved using SCMs [35]. These are based on a channel matrix $\mathbf{H} \in \mathcal{C}^{U \times S}$, with S (U) being the number of antenna elements at the transmitter (receiver) array. Each entry (i, j) in the matrix \mathbf{H} models the channel between two specific antenna elements, and represents the joint effect of different MPCs. Each MPC is characterized by angles of departure and arrival, power, and delay. The interaction with the antenna arrays can be modeled by pre- and post-multiplying to \mathbf{H} the beamforming vectors of the transmitter and receiver, respectively [23].

A popular class of SCMs is that in which the MPCs are generated from a set of random distributions, whose parameters are determined by statistical fits on channel measurements. The channel matrix thus has a stochastic nature, with the advantage that multiple instances can be randomly generated for generic, large scale scenarios. The random variables of these models are used to characterize two phenomena, i.e., large scale fading, which depends on the scenario and the user mobility, and fast fading, which is given by small scale variations in power resulting from the interference among the MPCs.

Notable examples of stochastic channel models are those derived from WINNER and WINNER-II models [36], e.g., the 3GPP channel model for the system-level evaluation of 5G deployments [22]. These models have been extensively used in the performance evaluations of mmWave networks [37], and are also integrated with popular open source network simulators [38]. The NYU channel model for 28 GHz and 73 GHz is also based on a stochastic SCM [23].

Quasi-Deterministic Channel Models: The stochastic nature of the aforementioned channel models makes them generic: they can model a common rural or an urban scenario, but not a specific scenario (e.g., Times Square in NYC). Therefore, they do not provide an accurate model for the interactions of the mmWave propagation with a peculiar deployment, making them unfit for detailed planning and capacity studies in real-world contexts.

As discussed in Sec. I, RTs can, instead, provide extremely accurate propagation results in a given environment, provided that its characterization in the simulation is accurate enough. With respect to stochastic channels, an RT generates the exact MPCs that can arise from a direct or reflected propagation path in the scenario [25]. Ray-Tracers have thus been the basis for several performance evaluation studies at mmWaves [26], [39], [40]. RT-based channel models have also been adopted as candidates for the evaluation of IEEE 802.11ay networks, with a QD extension [41], [27] that combines the geometry-based MPCs and a number of random diffuse components that model the interaction of the mmWave signal with rough surfaces.

However, while being extremely precise, RTs and QD models are also more computationally intensive than stochastic models for the generation of a single channel instance, especially if the number of scattering and reflecting surfaces in the scenario is large. While a number of optimizations have been studied for RTs in general [42], in the remainder of this paper we analyze the complexity of the considered open source mmWave RT and QD model, and propose ready-to-use recipes to reduce it, with specific focus on preserving the accuracy of system-level simulation results.

III. RAY-TRACING AT MILLIMETER WAVES

As previously discussed, ray-tracing is widely used to accurately simulate electromagnetic (EM) propagation in an environment, whose geometry is described by a Computer-Aided Design (CAD) model [43]. The fundamentals of this technique are derived by solving Maxwell's equations for the far field in the high-frequency regime, where the EM wave exhibits ray-like properties, i.e., the flow of power propagates in a straight line and reflects specularly on locally

flat surfaces. In practice, the high-frequency regime is assumed whenever the wavelength of the signal is much shorter than the typical size of obstacles in the scenario. In this case, secondary effects, i.e., diffraction, diffuse scattering, polarization, and refraction, should also be accounted for.

Some of these effects can be particularly significant in the propagation of mmWave signals. In this frequency band, the shorter wavelength leads to a higher effective roughness of the surfaces, thus increasing the amount of scattered power and, consequently, the reflection loss. The effect is twofold: on one side, higher-order reflections are expected to be weaker and thus affect the communication less than at lower frequency but, on the other side, proper modeling of the scattered rays should be taken into consideration [44]. Conversely, higher penetration loss will reduce received power in the cluttered areas, improving frequency reuse and reducing the cross-interference between close-by radiators. Finally, diffraction shadows are deeper at higher frequency, making diffraction a less prominent means of propagation in the mmWave band.

In this section, we describe the tools we use in this work to simulate the mmWave channel. Specifically, in Sec. III-A we describe the architecture and the assumptions of the RT used in this paper, while in Sec. III-B we briefly describe the diffuse scattering model.

A. *The Millimeter Wave Ray-Tracer*

For the results of this paper, we use an open-source RT developed jointly by the SIGNET group at the University of Padova and the U.S. National Institute of Standards and Technology (NIST). It uses triangles described in CAD files as the basic 3D surface element unit, which can then be combined to define complex shapes.

The RT only supports specular reflections and, optionally, diffuse scattering, ignoring effects such as diffraction, penetration, and polarization. The latter is not considered to further simplify the software from the Fresnel equations, which dictate the laws of reflection. The reflected rays thus experience a 180° phase rotation and a random reflection loss RL between 7 dB and 25 dB, depending on the material, but irrespective of the angle of incidence.

Multiple network nodes, playing the role of TXs and RXs, are modeled as points, and can be deployed simultaneously, allowing the calculation of interfering channels. Furthermore, trace-based mobility is supported, making it possible to create complex scenarios with multiple base stations and mobile users. Given N nodes and t time-steps, the simulator computes a channel

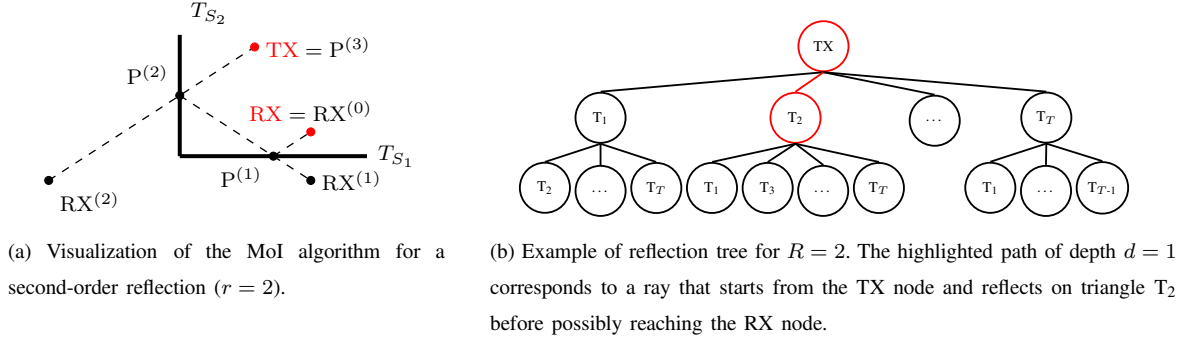


Fig. 1: Visualization of the basic principles behind the RT software used.

instance for each time-step and for each node pair. Considering a symmetric channel for a given node pair, $tN(N - 1)/2$ channel instances have to be calculated.

The RT uses the MoI [43] to compute specular reflections, assumed to be independent across time and node pairs. For the simplest case, i.e., first order reflections, the MoI defines the virtual image of a node, for example the RX , to be a specular image with respect to a surface. Formally, $RX^{(1)}$ is the specular image of the RX , defined as $RX^{(0)}$, across the surface S . The specular reflection point $P^{(1)}$ between the RX and the TX coincides with the intersection of the segment $(RX^{(1)}, TX)$ with the surface S , as shown in Fig. 1a.

Since triangles are used as the basic surface units of the CAD environment, S_i is the plane generated by a given triangle T_i , $i = 1, \dots, T$, where T is the total number of triangles of the CAD environment, and it must be verified that $P^{(1)}$ is a point within the area shaped by T_i , otherwise the reflection will not be valid and will thus be discarded. Finally, every segment of the ray, namely $(RX^{(0)}, P^{(1)})$ and $(P^{(1)}, TX)$, has to be checked against the remaining triangles of the environment T_j , $j = 1, \dots, T$, $j \neq i$ for obstruction. If any segment of the ray is obstructed, the whole ray is considered obstructed and thus discarded.

The MoI applies recursively when multiple reflections are considered, computing the n -th virtual image of the RX , $RX^{(n)}$, and the respective specular reflection point $P^{(n)}$ as shown in Fig. 1a. Thus, for each ray of reflection order $r > 0$, r geometrical operations must be done to compute the ray path and, if the ray is valid, each of the $r + 1$ segments needs to be checked for obstruction over the $T - 1$ triangles of the CAD environment. This totals to about $r + (r + 1)T$ operations per ray, for $T \gg 1$.

To compute all possible reflections between a given node pair, all possible paths have to be computed and tested for obstruction. Considering increasing reflection orders, the first one to be

tested is the direct ray, meaning the segment (RX, TX). Subsequently, all first order reflections are computed, meaning those rays starting from the TX, reflecting off a triangle T_i , $i = 1, \dots, T$ and reaching the RX. Then, second order reflections starting from the TX, reflecting first on triangle T_{i_1} , $i_1 = 1, \dots, T$ and then on triangle T_{i_2} , $i_2 = 1, \dots, T$, $i_2 \neq i_1$ to finally reach the RX, and so on up to a maximum reflection order R .

All the reflections can be encoded in a *reflection tree*, as represented in Fig. 1b, where each node of the tree corresponds to a possible ray, the node depth corresponds to the reflection order r starting from 0 from the root of the tree, and the path starting from the root describes the ordered tuple of reflecting triangles to be tested.

The complexity of a single channel instance, then, is determined by the total number of operations required for all the nodes of the reflection tree. At depth $r = 0$ we consider only the direct ray, at depth $r = 1$ we consider the T possible first-order reflections, then, in general, at depth $r \geq 2$ we consider $T(T - 1)^{r-1} < T^r$ possible r -order reflections. The total number of operations per channel instance is thus upper bounded as

$$\begin{aligned} \sum_{r=0}^R (r + (r + 1)T)T^r &= T \sum_{r=0}^R T^r + (T + 1) \sum_{r=0}^R rT^r \\ &= T \frac{T^{R+1} - 1}{T - 1} + (T + 1) \frac{T(RT^{R+1} - (R + 1)T^R + 1)}{(T - 1)^2} \xrightarrow{T \rightarrow \infty} T^{R+1} + RT^{R+1}, \end{aligned} \quad (1)$$

thus denoting a complexity per channel instance equal to $\mathcal{O}(RT^{R+1})$, and a total complexity equal to $\mathcal{O}(tN^2RT^{R+1})$. The last step in Eq. (1) is justified by considering that typical values for R and T are in the order of 1–4 and 100–10 000, respectively, thus making T the dominating term of the formula.

B. Quasi-Deterministic Model Integration

Besides the deterministic RT, in Sec. V we also evaluate the performance with and without a stochastic model for diffuse components, which alone can account for up to 40% of the total received power according to measurements campaigns [27]. It is based on the specifications proposed for IEEE 802.11ay channel modeling [45] with parameters obtained from accurate measurement campaigns [27]. Further details are given in [46]. Please note that in this section, boldface letters denote random variables while non-boldface letters denote deterministic variables or realizations of random variables.

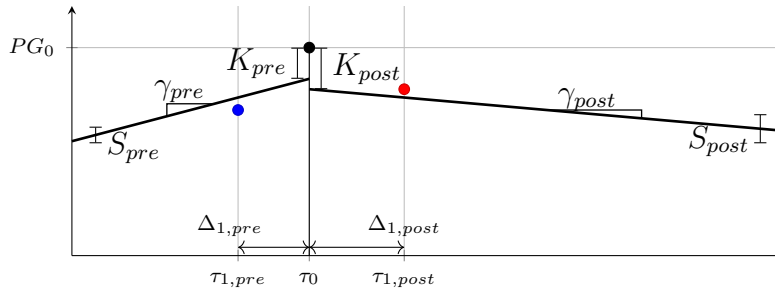


Fig. 2: Graphical representation of the QD parameters.

The QD model is built upon the deterministic channel, as described in Sec. III-A. For first-order reflections, the path gain of the Deterministic Ray (D-Ray) is equal to

$$PG_{0,\text{dB}} = 20 \log_{10} \left(\frac{\lambda_c}{4\pi \ell_{\text{ray}}} \right) - \mathbf{RL}_{\text{dB}}, \quad (2)$$

where λ_c is the wavelength of the carrier frequency, ℓ_{ray} is the total ray length, and $\mathbf{RL} \sim \mathcal{R}(s_{\text{RL}}, \sigma_{\text{RL}})$ is the Rician-distributed random reflection loss factor given by the reflecting surface's material, whose parameters have been fitted from measurements. The computed D-Rays will then be the baseline for the multipath components randomly generated by the QD model. If present, the direct ray is treated separately as it does not generate any diffuse component. For first-order reflections, a cluster can then be defined as the set of rays including a D-Ray and its diffuse components. The total number of MPCs of a given cluster will be $N_{\text{MPC}} = N_{\text{pre}} + 1 + N_{\text{post}}$, including pre-cursors (i.e., diffuse components that are received before the D-Ray), main cursor (i.e., the D-Ray), and post-cursors (i.e., received after the D-Ray).

The arrival time of the i -th MPC τ_i is modeled as a Poisson process, meaning that their inter-arrival times are independent and exponentially distributed, with an exponential power law, i.e.,

$$PG_i = \frac{PG_0}{\mathbf{K}} \cdot \exp \left(-\frac{|\tau_i - \tau_0|}{\gamma} + \mathbf{S} \right), \quad (3)$$

where $\mathbf{K}_{\text{dB}} \sim \mathcal{R}(s_{\text{K}}, \sigma_{\text{K}})$ is a loss factor, τ_0 is the D-Ray arrival delay, $\gamma \sim \mathcal{R}(s_{\gamma}, \sigma_{\gamma})$ is the power-delay decay constant, $\mathbf{S} \sim \mathcal{N}(0, \sigma_{\mathbf{S}}^2)$ is the power-delay decay standard deviation, and $\sigma_{\mathbf{S}} \sim \mathcal{R}(s_{\sigma_{\mathbf{S}}}, \sigma_{\sigma_{\mathbf{S}}})$. A graphic representation of these parameters is shown in Fig. 2.

Finally, the departure and arrival angles follow a Laplacian distribution around the D-Ray, while the phase shift ϕ_i due to both diffusion and Doppler shift is assumed to be $\mathcal{U}[0, 2\pi)$ independently for each diffuse MPC.

In general, for the r -th reflection order, with $r > 1$, the definitions presented above are heuristically adapted, considering independent statistics for the different reflectors. To reduce the

computational complexity of the complete model, the multi-bounce model neglects diffuse rays beyond the first order, given their fast increasing attenuation. Instead, only diffuse rays generated directly by the deterministic ray are taken into account, each generated with the QD parameters relative to the impinging reflecting surface. Moreover, we assume that every diffuse component closely follows the main cursor, thus reflecting on the same reflectors. Consequently, every reflector produces $N_{\text{pre}} + N_{\text{post}}$ diffuse components, thus yielding $N_{\text{MPC}} \sim r(N_{\text{pre}} + N_{\text{post}}) + 1$. Finally, diffuse components are independently extracted at each timestep.

IV. MMWAVE CHANNEL SIMPLIFICATIONS

The accuracy of the MoI-based ray-traced channels — especially when considering the QD model — comes at a high computational cost, which may limit the scalability of the simulations, especially when considering a very large number of devices. In this perspective, the main objective of this work is to evaluate how channel simplifications affect the results of link-level and network-level simulations while speeding-up the overall simulation runtime. In this section, we present two techniques that were designed with this objective in mind [24], starting from the analysis of the complexity discussed in Sec. III-A.

The overall computational complexity of a simulation of N TX/RX nodes lasting t time steps in a scenario composed of T triangles when considering up to R reflections is $\mathcal{O}(tN^2RT^{R+1})$. In this approach, t and N are simulation parameters set by the user, T is determined by the CAD model of the simulated environment, while the maximum reflection order R for the ray-tracing depends on the channel model. Understanding how different values of R affect the low- and high-layer performance metrics of the network with respect to the model complexity is the core of the first simplification strategy proposed in this work, referred to as *Maximum Reflection Order Reduction* (see Sec. IV-A).

Differently, the second technique aims at reducing the number of rays between a pair of nodes. Specifically, given a set of M rays connecting two nodes, we propose and evaluate a selection criteria that aims to reduce the number of MPCs to $M' < M$, to reduce the overall simulation time. This operation, named *MPC Thresholding*, is applied on a time-step basis (see Sec. IV-B).

The rationale behind both strategies is to decrease the number of MPCs by removing the least significant ones, i.e., those with the lowest power, as they are expected to provide a limited contribution to the overall received signal strength. More details will be given in the following subsections.

A. Maximum Reflection Order Reduction

Each reflection of the MPCs on a surface is associated to a partial power loss and an increased path length, translating into a higher path loss. Namely, from Eq. (2), the path gain for a ray reflected on r surfaces is

$$PG_{\text{dB}} = 20 \log_{10} \left(\frac{\lambda_c}{4\pi \sum_{i=1}^r \ell_i} \right) - \sum_{r=1}^r RL_{i,\text{dB}}, \quad (4)$$

where ℓ_i is the length of the segment associated with the i -th reflection. The summation is decomposed into two terms to underline the different contributions: both the path length and the reflection losses degrade the path gain when the reflection order increases. Therefore, it is reasonable to assume that MPCs that bounce across multiple scattering surfaces have a low contribution to the overall received power, and can be omitted from the RT computations. Setting the maximum reflection order to $R' < R$, the RT complexity is decreased to $\mathcal{O}(tN^2R'T^{R'+1}) < \mathcal{O}(tN^2RT^{R+1})$ with significant savings in terms of computation time, given the super-exponential dependency of the complexity on R .

B. MPC Thresholding

Beside the reflection order, there are other elements that contribute to reducing the MPC path gain. For example, even if R is small, in large scenarios surfaces that are located far from the TX and RX nodes are associated to MPCs with a large path length (i.e., the first term in Eq. (4)). As the path gain from these scatterers is much smaller than that from close-by reflecting surfaces, it is possible to prune them from the list of MPCs to compute.

For these MPCs, the path gain plays a key role and can thus be used as an indicator to perform the selection of the most significant rays. Specifically, the selection is performed at each time step considering a threshold γ_{th} , according to the following rules:

- the strongest ray is identified and the corresponding path gain PG_{strong} is computed;
- all the other MPCs are identified. Note that $PG_i < PG_{\text{strong}}$ for every MPC i .
- the selection is carried out discarding every MPC i such that $PG_i - PG_{\text{strong}} < \gamma_{\text{th}}$.

While being more general than the previous approach, as it tackles directly the weakest, least significant rays, this strategy requires the computation of all the geometric paths in order to obtain the path gain list. However, this method, which removes $(M - M')$ rays, eases the load on the subsequent RT operations, i.e., the obstruction check, reducing by a factor of $\frac{M-M'}{M}$ the complexity of each time step. In fact, following the same logic as in Sec. III-A for every ray

of reflection order r , after the r geometrical operations required to compute the path of the ray, none of the $(r + 1)T$ obstruction checks are performed if the ray is discarded. Updating Eq. (1) with $r \geq 0$ instead of $r + (r + 1)T$ operations per ray, the complexity can be reduced to $\mathcal{O}(tN^2RT^R)$ and thus by a factor up to T . Note that, whereas this approach achieves a constant factor improvement, T can be in the order of tens to thousands, depending on the details included in the CAD file and on the adopted triangulation, thus being one of the dominant terms in the complexity expression.

Absolute thresholding can also be used to limit the number of extremely weak rays similarly to the previous technique. This approach can be useful when considering high values for R , low values for γ_{th} , and especially when using the QD model. In this case, setting a threshold Γ_{th} , every MPC i such that $PG_i < \Gamma_{\text{th}}$ is discarded.

The complexity of the RT can be significantly reduced thanks to the removal of MPCs and to the reduction of the maximum reflection order R . On the other hand, these simplifications degrade the accuracy of the simulation results at the different levels of the network stack. In the remainder of this paper, we will quantify this trade-off for three realistic propagation scenarios. The overall end-to-end network performance and the runtime of the simplified RT settings will be compared with those of the complete, non-simplified channel traces.

V. PERFORMANCE EVALUATION

This section reports the details of an extensive performance evaluation aimed at understanding the impact that the simplifications introduced in Sec. IV have at different layers of the protocol stack. We first describe the scenarios and tools used for the performance evaluation (Sec. V-A), then the link and higher layer performance (Secs. V-B and V-C, respectively), and conclude with the computational performance given by the simplifications (Sec. V-D) and guidelines for the more efficient design configurations (Sec. V-E).

A. Simulation Scenarios

Three representative scenarios with distinctive features have been selected to make the performance evaluation as general as possible. Their main characteristics are hereby described, and are summarized in Table I. Without loss of generality, only downlink channels are considered.

- 1) *Indoor1*: The most basic scenario, with a rectangular room (see Fig. 3a) of size $10 \text{ m} \times 19 \text{ m} \times 3 \text{ m}$. The TX is positioned close to the ceiling at $(5, 0.1, 2.9) \text{ m}$. The RX, at height

TABLE I: Characteristics of the simulated scenarios. Other important simulation parameters are bandwidth $B = 400$ MHz, and noise figure $NF = 9$ dB. All nodes of a given scenario transmit with the same power P_{tx} .

Scenario	Time steps t	LoS	NLoS	Environment	RX velocity	Interferer	T	P_{TX}
Indoor1	3133	✓	✗	Indoor	1.2 [m/s]	✗	12	20 dBm
L-Room	3831	✓	✓	Indoor	1.2 [m/s]	✓	16	20 dBm
ParkingLot	3971	✓	✗	Outdoor	4.17 [m/s]	✓	284	30 dBm

1.5 m, moves away from it at a speed of 1.2 m/s along a straight line. This scenario was deliberately designed to be simple, to analyze the propagation characteristics simulated by the RT focusing on the received power pattern when different simplifications are used;

- 2) *L-Room*: An L-shaped hallway (see Fig. 3b). A static TX, placed at (0.2, 3, 2.5) m, transmits to the reference RX that moves away from it at a speed of 1.2 m/s across the corridor. The shape of the room is such that the RX is in NLoS condition for a significant portion of the path. Moreover, in order to analyze the impact of interference on the network performance, a second TX placed at (8, 18.8, 2.5) m and acting as interferer, communicates with an RX at (9, 3, 1.5) m. Furthermore, the shape of the room plays an important role when comparing the proposed simplification techniques, as it may create blind spots where no signal is received;
- 3) *Parking-Lot*: The only outdoor scenario, representing a parking area of about 120 m \times 70 m enclosed by buildings (see Fig. 3c). The reference TX transmits from an access point placed at 3 m height on a building to the RX, that moves at a speed of 4.17 m/s (15 km/h) around the parking lot. By far the largest scenario, it makes it possible to analyze the effect of the simplifications in terms of time savings when the CAD file contains a large number T of triangles. Moreover, the reference RX moves at a much higher speed than in the previous scenarios, as in a basic vehicular scenario.

The ray-tracing parameters for the *Indoor1* [27] and for the *Parking Lot* scenarios are obtained from detailed measurement campaigns.

For each scenario, the RT and QD model software described in Sec. III have been used to generate the channel instances for the specified devices and mobility patterns sampled every 5 ms. These traces were then integrated in a custom MATLAB simulator [24], [1] to evaluate metrics at the link layer (e.g., the SINR), and with the mmWave module [29] of the ns-3 network simulator [28] to investigate the performance of the full protocol stack.

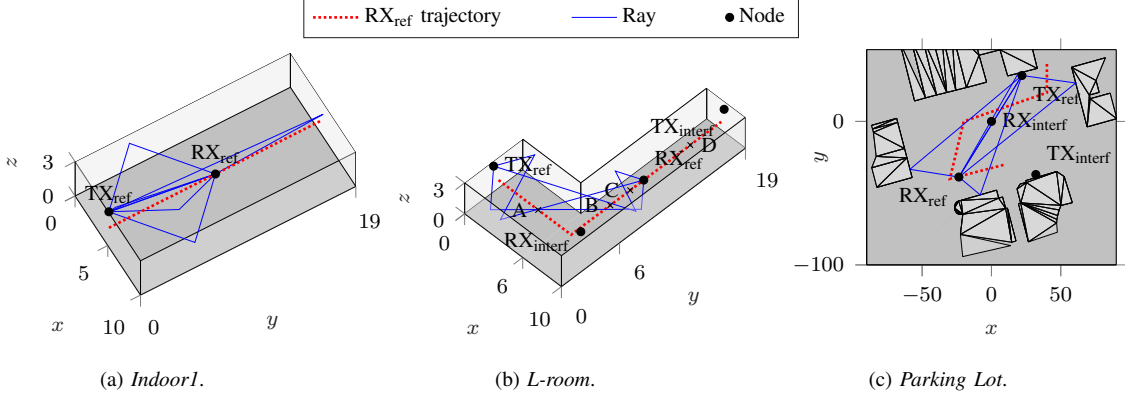


Fig. 3: Visual representations of our simulation scenarios. Distances are measured in meters.

Both simulators rely on the computation of the channel matrix \mathbf{H} to describe the channel obtained from the MPCs provided by the RT and QD. Given M rays, with path power gain PG_m , phase shift Φ_m , delay τ_m , and angles of departure \mathbf{AoD}_m and angles of arrival \mathbf{AoA}_m , the matrix for the carrier frequency f_c is computed as

$$\mathbf{H} = \sum_{m=1}^M \sqrt{PG_m} e^{j(-2\pi\tau_m f_c + \Phi_m)} \mathbf{a}_{\text{rx}}^*(\mathbf{AoA}_m) \mathbf{a}_{\text{tx}}^H(\mathbf{AoD}_m), \quad (5)$$

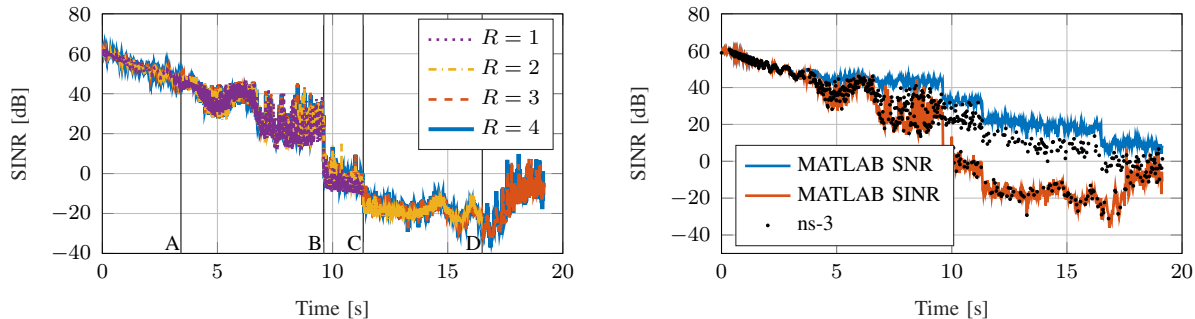
where $\mathbf{a}_{\text{rx}}(\boldsymbol{\theta})$ and $\mathbf{a}_{\text{tx}}(\boldsymbol{\theta})$ are the receiver and transmitter array responses in the 3D angle $\boldsymbol{\theta}$, $(\cdot)^*$ is the conjugate operator, and $(\cdot)^H$ is the Hermitian operator. The SINR for the link between the transmitter t and the receiver r is

$$\Gamma_{t,r} = \frac{P_{\text{tx},t} \mathbf{w}_{t,r}^T \mathbf{H}_{t,r} \mathbf{w}_{r,t}}{\sum_{m \neq t} P_{\text{tx},m} \mathbf{w}_{m,*}^T \mathbf{H}_{m,r} \mathbf{w}_{r,t} + N_0 B F}, \quad (6)$$

where $P_{\text{tx},t}$ is the transmit power of device t , $\mathbf{w}_{i,j}$ is the beamforming vector used by device i to communicate with device j (and $\mathbf{w}_{i,*}$ is used with abuse of notation to indicate the beamforming vector used by device i to transmit towards a connected device, or $\mathbf{0}$ if i is not transmitting), N_0 is the noise power spectral density, B is the bandwidth, and $F = 10 \frac{NF}{10}$ is the noise factor of the receiver.

For ns-3, we extended the channel model implementation described in [38] to account for a generic channel matrix computed, in this case, as expressed in Eq. (5)². In the performance evaluation, this channel model has been combined with the 3GPP-like protocol stack of the 5G mmWave module for ns-3 [29], which features physical and Medium Access Control (MAC) layers with an Orthogonal Frequency Division Multiplexing (OFDM)-based frame structure, dynamic Time Division Duplexing (TDD), Adaptive Modulation and Coding (AMC), and several

²The implementation can be found at <https://github.com/signetlabdei/qd-channel>.

(a) SINR vs. time for different values of R , with $\gamma_{\text{th}} = -\infty$ dB.

(b) SINR vs. time considering MATLAB and ns-3 simulations.

Fig. 4: Evolution of the SINR experienced when the test RX moves in the L -room scenario along the path described in Fig. 3b.

scheduler implementations. Besides, the User Equipments (UEs) and base stations protocol stacks are completed by 3GPP Radio Link Control (RLC) and Packet Data Convergence Protocol (PDCP) layers, together with a realistic control plane based on the Radio Resource Control (RRC) layer which supports mobility-related procedures [47]. We consider two configurations for the uniform planar antenna arrays: large arrays, comprising 8×8 elements for the TXs and 4×4 elements for the RXs, and small arrays, comprising 2×2 arrays for both TXs and RXs, all of them with omni-directional elements spaced apart by $\frac{\lambda}{2}$. The planes on which all planar arrays lie are parallel to the y - z plane with a fixed orientation throughout the simulation. Finally, thanks to the integration with ns-3, it is possible to equip the UEs with the TCP/IP stack and applications which connect to remote servers in the Internet.

The results shown in the following sections will assume as default parameters, unless stated differently, a maximum reflection order $R = 3$ for the *Parking Lot* scenario, and $R = 4$ for the others, a relative threshold $\gamma_{\text{th}} = -\infty$ dB, a conservative absolute threshold $\Gamma_{\text{th}} = -200$ dB, a large antenna array configuration, only deterministic rays (i.e., no QD model), and a UDP stream with an offered traffic equal to 800 Mbps. The beamforming is based on the Singular Value Decomposition (SVD) of the channel matrix \mathbf{H} .

B. Link-Level Performance Results

The first step towards proper protocol design is gaining a deep understanding of how the proposed ray-tracing simplifications impact the link-level performance of the network, neglecting, at this stage, the effects at the upper layers. In this perspective, we are interested in investigating how the strategies described in Sec. IV result in different SINR regimes.

From Fig. 4a, which plots the temporal evolution of the SINR experienced when the RX moves in the *L-Room* scenario along the path described in Fig. 3b, it is possible to see that the impact of R is certainly non-negligible: the trend of the SINR visibly changes when progressively reducing the number of reflections per MPC. Moreover, we see that the SINR evolves consistently with the mobility of the RX. The SINR indeed drops by more than 30 dB when the RX loses its LoS condition (position B in Fig. 3b), while the SINR degradation that is experienced at time $t = 3.4$ s (position A in Fig. 3b) is due to the interference from the RX_{interf} . Rapid fluctuations within the SINR trace are then due to the fact that different MPCs travel different paths. At 60 GHz, where the wavelength is as short as $\lambda = 5$ mm, even small variations of the path length between the direct ray and the reflected ones from the back wall (behind the TX), side walls, ceiling, and floor of the room, may result in strong fading. Fig. 4a also shows that the impact of the RT simplifications is particularly evident when the RX operates in NLoS: in this region, in fact, the received power drops to zero when first-order and second-order reflections are removed (positions C and D in Fig. 3b, respectively).

For completeness, in Fig. 4b we compare the metrics from the MATLAB (straight lines) and the ns-3 (dots) simulations. The MATLAB SINR assumes an always-on interferer, representing a lower bound for the SINR metric, while the MATLAB Signal-to-Noise Ratio (SNR) metric assumes an interference-free channel. On the other hand, ns-3 models a realistic transmission pattern for the primary and interferer links, which could occupy the channel in overlapping, partially overlapping, or non-overlapping time instants. Therefore, for each time instant, the SINR generated by the ns-3 simulations is lower and upper bounded by the MATLAB SINR and SNR, respectively. On the other hand, if the reference TX and the second TX/RX pair communicate in non-overlapping time slots, interference is minimized and the ns-3 SINR curve closely approximates the MATLAB configuration without interferer.

The same conclusions can be drawn from Fig. 5, which illustrates the Cumulative Distribution Function (CDF) of the SINR for the three scenarios described in Sec. V-A as a function of R . Specifically, the *L-Room* scenario, due to the presence of NLoS conditions, is again the only one for which a reduction of the MPCs of the channel may result in a significant reshape of the CDF of the SINR with respect to the baseline configuration with no simplifications. On the other hand, both the *Indoor1* and the *Parking Lot* scenarios are able to preserve the LoS for the whole duration of the simulation, thereby making it possible for the signal to propagate with a minor impact on the received power even when limiting the number of reflections R per MPC.

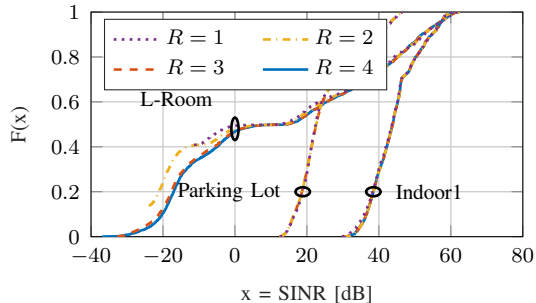


Fig. 5: Cumulative Distribution Function of the SINR in different scenarios vs. R , with $\gamma_{th} = -\infty$ dB.

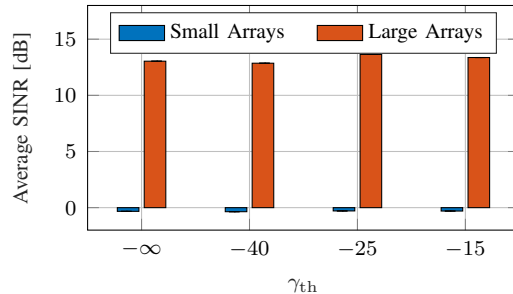


Fig. 6: Average SINR vs. γ_{th} as a function of the antenna architecture in the *L-Room* scenario, with $R = 4$.

Notice that the 20 dB gap of SINR between the *Parking Lot* and the *Indoor1* configurations is due to the larger distance between the TX and the RX, and to the reflecting surfaces (e.g., buildings) in the outdoor scenario.

Finally, in Fig. 6 we plot the SINR vs. the relative threshold γ_{th} as a function of the antenna size at the TX and the RX. As expected, the SINR increases when increasing the number of antenna elements, which increases the beamforming gain. Also, while the impact of R severely affects the SINR in the *L-Room* scenario, increasing the relative threshold γ_{th} to reduce the number of MPCs to be processed by the RT has negligible deterioration at the link-level, while speeding up the simulation, as will be discuss in Sec. V-D.

C. End-to-End Performance Results

Many of the conclusions we derived from the link-level performance metrics in Sec. V-B can be extended to the end-to-end ones, namely throughput and delay at the PDCP layer. Statistics have been collected at this layer since they can easily profile both UDP and TCP traffic indistinctly and are very close to the application layer performance, without the addition of extra delays due to the specific architecture of the simulation scenario.

In this section we study three types of traffic, namely full-buffer TCP traffic and UDP traffic with a Constant Bit Rate (CBR) of 100 Mbps and 800 Mbps. The latter was chosen to be the default for the results shown in this section, unless stated differently. Both throughput and delay are averaged over 100 ms windows.

Fig. 7 reports end-to-end metrics over time for the *L-Room* scenario as a function of the maximum number of reflections R , making it possible to analyze the behavior at specific time instants. First of all, we notice that the 800 Mbps data rate for UDP was chosen to saturate

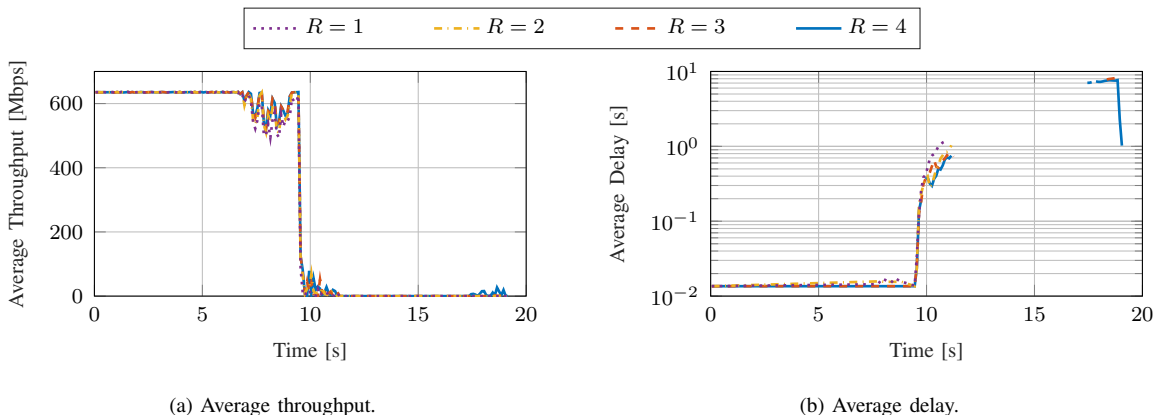
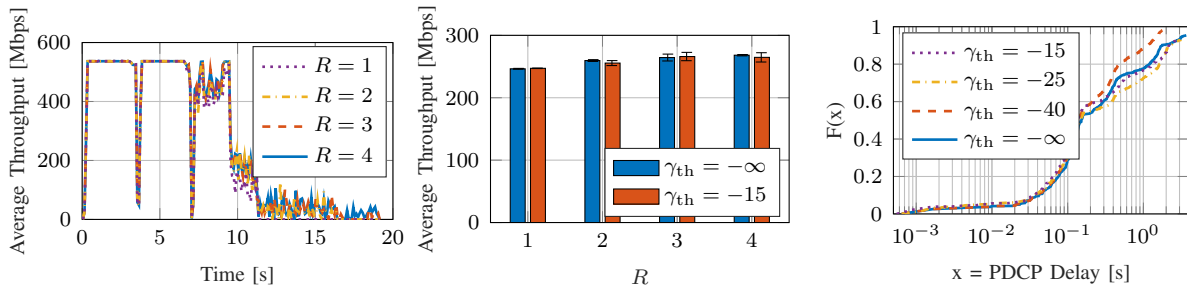


Fig. 7: End-to-end performance vs. R for the *L-Room* scenario with a UDP CBR traffic of 800 Mbps averaged over 100 ms windows.

the channel capacity, as the physical layer only supports 630 Mbps at peak performance. The interference starts to impact the UDP performance from 7 s, followed by a rapid performance degradation when the direct ray is lost in point B (see Fig. 3), at about 9.65 s. Between point B and point C (11.33 s), the signal is still strong enough to allow for some transmissions, resulting, however, in a rapid increase of the delay of received packets due to buffering and retransmissions. When RX_{ref} gets closer to TX_{interf} (i.e., around 17 s), the interference decreases enough to still support data communication, although with extremely high delay, but only for R large enough to reach the end of the corridor, i.e., $R \geq 3$. As a matter of fact, TX_{interf} points its 64 antenna elements towards RX_{interf} , in LoS at the end of the corridor. Thus, when RX_{ref} gets closer to the source of the interference, the angular separation with respect to RX_{interf} is large enough to reduce the received interfering power due to the highly directional communication of the interfering TX, resulting in an increased SINR. In this case, the second-order reflections between points C and D cannot alone guarantee a sufficiently high SINR for the transmission, given the significant amount of interference.

Fig. 8a shows the corresponding simulations using a full-buffer TCP traffic stream, which reaches 536 Mbps at peak. As expected, sudden jumps in the channel quality lead to sudden performance drops in TCP. This is the case in point A at 3.415 s (see Fig. 3), where the strong first-order rays of TX_{interf} are received by RX_{ref} , at the beginning of the interfering regime at about 7 s, when the direct ray is lost in point B at 9.65 s, and finally when the strong first-order reflections are lost in point C at 11.33 s.

For these reasons, Fig. 8b highlights a positive correlation between the average throughput and the maximum reflection order R , although only a 9% increase is observed with $\gamma_{\text{th}} = -\infty$ dB,

(a) Throughput over time, $\gamma_{th} = -\infty$ dB.

(b) Average throughput.

(c) PDCP delay, $R = 4$.Fig. 8: End-to-end performance vs. R and γ_{th} for the *L-Room* scenario with full-buffer TCP traffic.

going from 246 Mbps for $R = 1$ to 268 Mbps for $R = 4$. In general, instead, delay statistics do not show a clear trend in the reflection order, nor in the relative threshold, probably due to the extra complexity created by retransmissions and queues. An example is shown in Fig. 8c where most statistics follow a very similar trend, separating only towards extreme values of delay, corresponding to the portion of the scenario after point B, i.e., when the direct ray is lost. Notice that the CDFs for the delay do not reach 1 since windows where no packets were received were considered to have infinite average delay.

Unlike for the UDP case at 800 Mbps, TCP decreases the congestion window when strong interference affects the communication for both the reference and the interfering streams. For this reason, packets sent during the interfering regime do not always collide with each other. The reduced interference greatly increases the perceived SINR, as explained in Sec. V-B for Fig. 4b, thus triggering transmissions even after point B for $R \geq 2$. Although not shown here, similar conclusions can be drawn for UDP traffic at 100 Mbps, which is able to transmit after point B as well, sending data at a rate that depends on the small scale fading affecting the communication.

A comparison between a purely-deterministic and a quasi-deterministic channel with the QD model described in Sec. III-B is shown in Fig. 9. In general, from Fig. 9a it is possible to notice that the added random rays from the QD model tend to (i) increase the average received power and (ii) increase the frequency and amplitude of power fluctuations due to small scale fading, which is considered independent across subsequent time steps of 5 ms at a speed of 1.2 m/s. These fluctuations can also affect the end-to-end performance, making it significantly less stable.

To further study these random fluctuations, the CDF of the standard deviation of the throughput over 100 ms windows has been computed. To obtain this metric, we first computed the average throughput over 5 ms sub-windows, i.e., the sampling period chosen for the ray-traced channel, and subsequently the standard deviation over 20 consecutive sub-windows. This approach makes

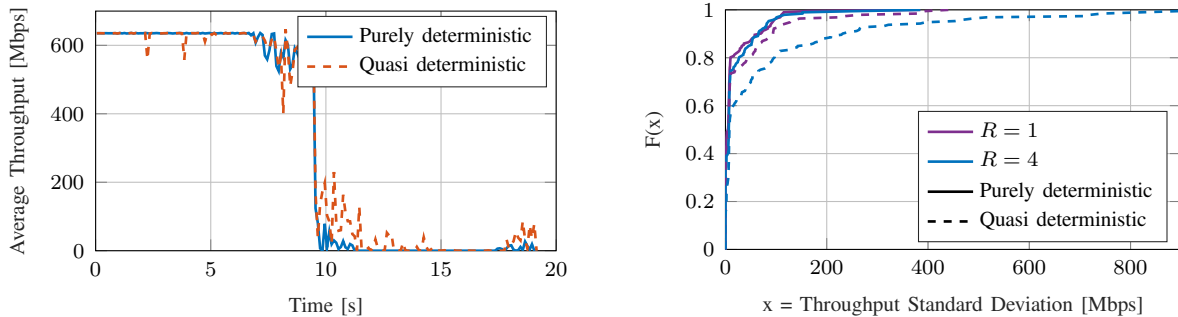
(a) Throughput over time with $R = 4$ and $\gamma_{\text{th}} = -\infty$ dB.(b) Throughput standard deviation for $\gamma_{\text{th}} = -\infty$ dB.

Fig. 9: Throughput performance for the *L-Room* scenario with a purely-deterministic and quasi-deterministic channel model, with a UDP CBR yielded traffic of 800 Mbps.

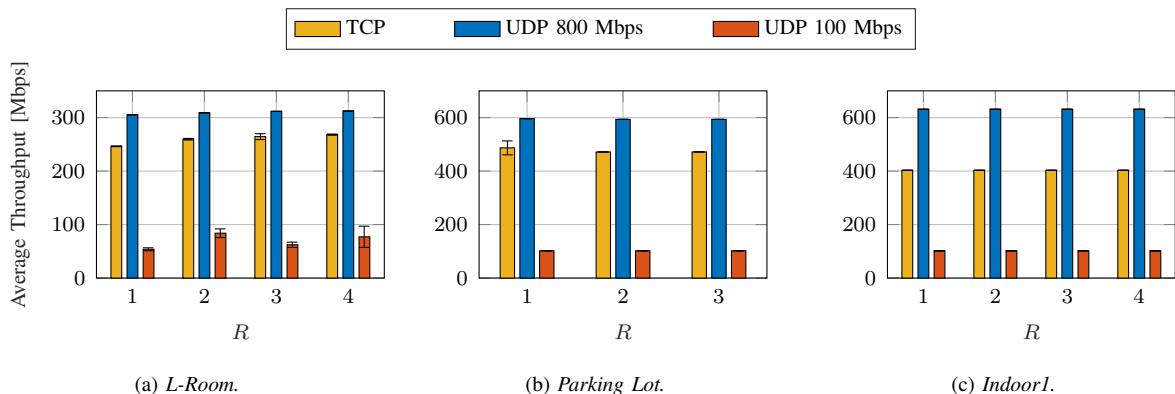
(a) *L-Room*.(b) *Parking Lot*.(c) *Indoor1*.

Fig. 10: Average throughput considering $\gamma_{\text{th}} = -\infty$ dB.

it possible to capture the deviation of the throughput over short time intervals, where it can be considered roughly constant. Computing the standard deviation over the whole simulation, in fact, would yield a misleading metric, given the extreme differences over the almost 20 s long scenario. Fig. 9b shows how an increasing number of rays tends to increase the standard deviation of the throughput due to an increased small scale fading, especially when a quasi-deterministic model with random diffuse components is considered. This effect should be taken into account when evaluating the performance of protocols for mmWave communications which adapt to the channel conditions, e.g., TCP [8].

The average throughput for different configurations is shown in Fig. 10, including the 95% Confidence Interval (CI), often extremely narrow. Both the LoS-only scenarios, namely *Parking Lot* and *Indoor1*, show virtually no variations across different values of R for all the three types of traffic considered. Minor variations can only be observed for the *L-Room* scenario, where the NLoS regime sets apart simulations with $R \leq 2$ from those with $R \geq 3$, not being able to exploit the last part of the path with lower interference and thus showing slightly lower performance.

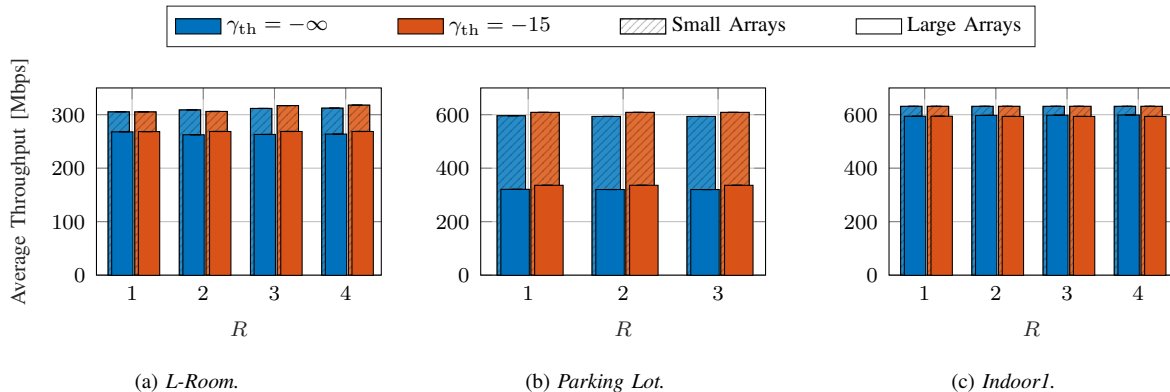


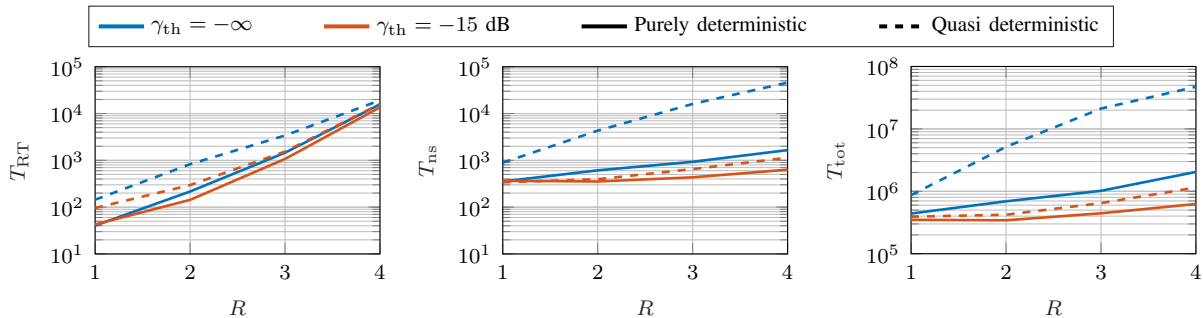
Fig. 11: Average throughput for the 800 Mbps traffic considering different antenna architectures.

Similar results are shown in Fig. 11, where two sets of antenna configurations are considered. When smaller antenna arrays, and thus smaller antenna gains, are simulated, the average performance of the system decreases for all scenarios. The largest performance hit is experienced by the *Parking Lot* scenario, since the stronger path loss experienced as a result of the larger propagation distances involved in the outdoor scenario can be mitigated by the antenna gain. The performance drop observed in Fig. 11 can be also due to stronger interference. Smaller arrays, in fact, are not able to create narrow beams, making $\text{TX}_{\text{interf}}$ interfere more strongly with RX_{ref} .

D. Computational Performance

The simulation techniques proposed in Sec. IV offer a trade-off between the simulation speedup given by the lower complexity, and a corresponding loss of accuracy. Secs. V-B and V-C analyzed in-depth the impact of the simplifications on the network metrics at two distinct levels. Here, we compare the proposed simplifications from a computational complexity point of view, and then draw guidelines on the optimal combination of parameters that maximizes the accuracy.

For completeness, we need to distinguish the different contributions to the total runtime T_{tot} required by a network simulation. The first is the RT runtime T_{RT} , required by the RT to generate the MPCs for the channel matrix. The second contribution, T_{ns} , is due to the network simulator (either MATLAB or ns-3 in this work), which includes the computation of the channel matrix with the RT data and what can be considered as simulation overhead. As the same RT channel trace can be used for an extensive simulation campaign, we define the overall runtime as $T_{\text{tot}} = T_{\text{RT}} + 1000 T_{\text{ns}}$, i.e., the time required to simulate one RT channel realization employed in 1000 network simulations, a typical if not conservative number when testing multiple parameters over multiple runs, e.g., for Monte Carlo analysis.



(a) Ray-Tracer runtime.

(b) Network Simulator 3 (ns-3) runtime.

(c) Total runtime.

Fig. 12: Simulation runtime vs. R and γ_{th} . The total runtime (Fig. 12c) accounts for an RT simulation (Fig. 12a) and 1000 ns-3 simulator runs (Fig. 12b). A purely-deterministic channel and a quasi-deterministic channel are considered.

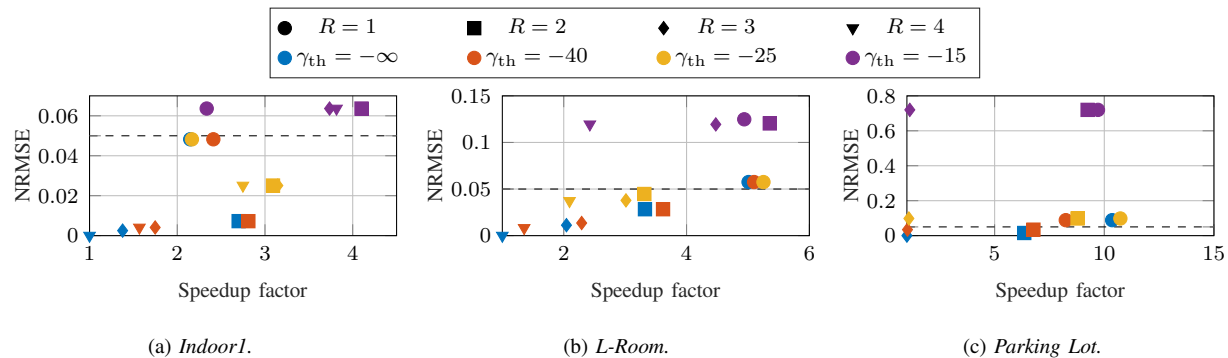
Fig. 12 shows the RT, the ns-3, and the corresponding total runtime, for the *L-Room* scenario. The figure compares the impact on the computational complexity of the simplification introduced by the reduction of the maximum order of reflection R . We consider the two extreme values of γ_{th} , i.e., -15 dB and $-\infty$ dB, and we compare a purely-deterministic channel with a quasi-deterministic channel that includes the random diffuse components introduced by the QD model. First, it can be observed that R has the greatest impact on the runtime. In particular, the RT runtime T_{RT} increases by more than 2 orders of magnitude when increasing R , and the ns-3 runtime T_{ns} experiences a similar effect. The impact of the QD model is clearly visible in Fig. 12b, and, consequently, in Fig. 12c. Nevertheless, note that in this case increasing the MPC thresholding γ_{th} to -15 dB can effectively reduce the gap between the runtime with and without QD model, for every reflection order.

Additionally, to summarize the conclusions from Secs. V-B and V-C quantitatively, we express the difference of the network performance between the simplified models and the baseline³ considering the Normalized Root Mean Square Error (NRMSE), computed as [1]

$$\text{NRMSE} = \frac{\text{RMSE}}{\sigma_{\hat{x}}} = \frac{\sqrt{\frac{1}{N} \sum_{n=1}^N [(x_n - \hat{x}_n)^2]}}{\sigma_{\hat{x}}}, \quad (7)$$

where x is the metric with the configuration of interest, \hat{x} is the baseline metric, and $\sigma_{\hat{x}}$ represents the standard deviation of the baseline metric. This metric evaluates the distance between each baseline-simplified pair of a given simulated metric in the time domain. Thus, it can detect punctual variations such as sharp drops or spikes, which may be relevant for communication

³Recall that the reference baseline is obtained without simplifications, i.e., with the maximum available reflection order for the scenario ($R = 4$ for *Indoor1* and *L-Room* and $R = 3$ for *Parking Lot*), and with $\gamma_{\text{th}} = -\infty$ dB.



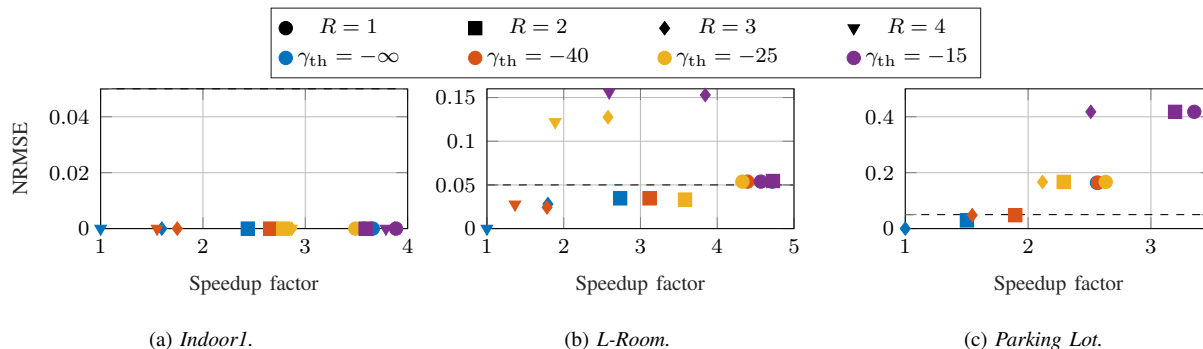


Fig. 14: Trade-off between the throughput performance and the speedup obtained with the different simplification parameters for the three scenarios. As in Sec. V-C, for the throughput ns-3 has been considered.

with respect to the previous case with $\gamma_{th} = -15$ dB. This is due to the higher absorption coefficient of the materials that are present in the outdoor environment, that, together with the increased path lengths, lead to a significant decrease in the average MPC power. Thus, a low γ_{th} severely degrades the overall received power by removing a large percentage (even up to 90%) of such MPCs, whose overall contribution is far from negligible. In this case, the best configuration would be $R = 2$ and $\gamma_{th} = -40$ dB, achieving a speedup of 6.8 with an NRMSE of 0.034.

End-to-End Performance: Fig. 14 reports the NRMSE of the throughput vs. the speedup for end-to-end simulations. Similarly to what happened for the link-level performance, γ_{th} shows diminishing returns especially for both the *L-Room* and the *Parking Lot* scenarios.

Fig. 14a shows that virtually no variations occur when introducing simplifications in the *Indoor1* scenario. This suggests that setting $R = 1$ and $\gamma_{th} = -15$ dB can speed up the simulation by a factor of almost 4 with negligible accuracy loss with respect to the baseline configuration.

Good results are obtained also for the *L-Room* scenario in Fig. 14b, and with $R = 2$ and $\gamma_{th} = -25$ dB it is possible to gain a 3.6 speedup factor with an NRMSE of 0.033, or even a 4.7 speedup if an NRMSE of 0.054 is still accepted using $R = 1$.

Similarly to the link-level case, the end-to-end simulations for the *Parking Lot* scenario in Fig. 14c are much more severely affected by the simplifications. With both $\gamma_{th} \geq -25$ dB and $R = 1$, the NRMSE increases beyond acceptable levels. Nevertheless, setting $R = 2$ and $\gamma_{th} = -40$ dB offers an NRMSE as low as 0.048 with a 1.9 speedup factor.

E. Design Guidelines

Without focusing on the exact numbers, that are specific to the scenarios and the simulation tools employed in this work, it is still possible to draw some general guidelines for an efficient RT simulation.

- *Environment.* The simulation scenario plays a key role in the simplification choice. Specifically, when considering indoor LoS simulations, the secondary rays can be neglected with good approximation and very significant time savings. When considering also NLoS conditions in indoor scenarios, instead, less flexibility should be expected, although it is still possible to consistently reduce the runtime with a minor accuracy loss. Finally, outdoor scenarios should be treated carefully, as aggressive simplifications can have detrimental effects on the fidelity of the simulations. Nevertheless, a working point can be identified which offers a significant speedup.
- *Simplification Strategy.* Although their effect can vary substantially depending on the considered scenario, some general considerations can be drawn regarding the simplification techniques. The link-level metrics, such as the SINR, benefit, in terms of runtime, more from a reduction of the maximum reflection order rather than from an increase of the MPC threshold. For both link-level and end-to-end metrics, an aggressive thresholding policy leads to a performance degradation that is not justified by a corresponding speedup improvement. Finally, end-to-end results require a balanced use of both simplification techniques to achieve an optimal working point. In general, it can be noticed that $R = 2$ and a relative threshold $\gamma_{\text{th}} = [-40, -25]$ dB consistently yield a good balance of accuracy and speedup in almost all cases, and for this reason it is the suggested configuration.

VI. CONCLUSIONS AND FUTURE WORK

Accurate and scalable simulations are the basis for the design and evaluation of future 5G networks operating at mmWave frequencies. The usage of large antenna arrays, however, requires the modeling of the spatial dimension of the channel, for example through RTs, which can model the propagation of the different multipath components of a mmWave signal based on the geometry of the scenario. In this paper, we discussed two possible simplification techniques to decrease the computational complexity of RT-based channel and network simulations, to improve the scalability of these techniques. We showed that, while the proposed strategies decrease the number of multipath components to be actually computed, they have a different impact on the

physical layer and end-to-end performance with different scenarios, applications, and antenna array configurations. We believe that the insights that resulted from the extensive profiling and performance evaluation can guide researchers in designing accurate, yet scalable, simulations of mmWave networks.

As future work, we plan to extend the profiling and comparison considering end-to-end measurements in actual mmWave deployments, reproducing the scenario in the RT. Moreover, we also plan to study the impact of the simplifications on different beamforming architectures (e.g., hybrid beamforming).

ACKNOWLEDGMENTS

We want to thank our collaborators at NIST for their support and for providing high-quality data. In particular, we want to thank (in alphabetical order) Anuraag Bodi, Camillo Gentile, Nada Golmie, Chiehping Lai, Tanguy Ropitault, Neeraj Varshney, Jian Wang.

REFERENCES

- [1] M. Lecci, P. Testolina, M. Giordani, M. Polese, C. Gentile, T. Ropitault, N. Varshney, A. Bodi, and M. Zorzi, "Simplified Ray Tracing for the Millimeter Wave Channel: A Performance Evaluation," in *IEEE Information Theory and Applications Workshop (ITA)*, Feb. 2020.
- [2] ITU-R, "IMT vision - Framework and overall objectives of the future development of IMT for 2020 and beyond," Recommendation ITU-R M.2083, Sep. 2015.
- [3] 3GPP, "NR; Overall description; Stage-2," 3rd Generation Partnership Project (3GPP), Technical Specification (TS) 38.300, Jan. 2018.
- [4] P. Zhou, K. Cheng, X. Han, X. Fang, Y. Fang, R. He, Y. Long, and Y. Liu, "IEEE 802.11ay-Based mmWave WLANs: Design Challenges and Solutions," *IEEE Communications Surveys and Tutorials*, vol. 20, no. 3, pp. 1654–1681, Third Quarter 2018.
- [5] 3GPP, "New WID on extending current NR operation to 71 GHz," Qualcomm, RP-193229 - 3GPP TSG RAN Meeting 86, Dec. 2019.
- [6] T. S. Rappaport, S. Sun, R. Mayzus, H. Zhao, Y. Azar, K. Wang, G. N. Wong, J. K. Schulz, M. Samimi, and F. Gutierrez, "Millimeter wave mobile communications for 5G cellular: It will work!" *IEEE Access*, vol. 1, pp. 335–349, 2013.
- [7] S. Sun, T. S. Rappaport, R. W. Heath, A. Nix, and S. Rangan, "MIMO for millimeter-wave wireless communications: Beamforming, spatial multiplexing, or both?" *IEEE Communications Magazine*, vol. 52, no. 12, pp. 110–121, Dec. 2014.
- [8] M. Zhang, M. Polese, M. Mezzavilla, J. Zhu, S. Rangan, S. Panwar, and M. Zorzi, "Will TCP Work in mmWave 5G Cellular Networks?" *IEEE Communications Magazine*, vol. 57, no. 1, pp. 65–71, January 2019.
- [9] J. S. Lu, D. Steinbach, P. Cabrol, and P. Pietraski, "Modeling human blockers in millimeter wave radio links," *ZTE Communications*, vol. 10, no. 4, pp. 23–28, 2012.
- [10] M. Giordani, M. Mezzavilla, A. Dhananjay, S. Rangan, and M. Zorzi, "Channel dynamics and SNR tracking in millimeter wave cellular systems," in *22nd European Wireless Conference*, 2016.

- [11] M. Giordani, M. Polese, A. Roy, D. Castor, and M. Zorzi, "A tutorial on beam management for 3GPP NR at mmWave frequencies," *IEEE Communications Surveys and Tutorials*, vol. 21, no. 1, pp. 173–196, First Quarter 2019.
- [12] M. Giordani, M. Mezzavilla, and M. Zorzi, "Initial access in 5G mmWave cellular networks," *IEEE Communications Magazine*, vol. 54, no. 11, pp. 40–47, Nov. 2016.
- [13] S. Sun, T. S. Rappaport, M. Shafi, P. Tang, J. Zhang, and P. J. Smith, "Propagation models and performance evaluation for 5G millimeter-wave bands," *IEEE Transactions on Vehicular Technology*, vol. 67, no. 9, pp. 8422–8439, Jun. 2018.
- [14] S. K. Saha, Y. Ghasempour, M. K. Haider, T. Siddiqui, P. D. Melo, N. Somanchi, L. Zakrajsek, A. Singh, R. Shyamsunder, O. Torres *et al.*, "X60: A programmable testbed for wideband 60 GHz WLANs with phased arrays," *Computer Communications*, vol. 133, pp. 77–88, Jan. 2019.
- [15] M. Polese, F. Restuccia, A. Gosain, J. Jornet, S. Bhardwaj, V. Ariyaratna, S. Mandal, K. Zheng, A. Dhananjay, M. Mezzavilla, J. Buckwalter, M. Rodwell, X. Wang, M. Zorzi, A. Madanayake, and T. Melodia, "MillimeTera: Toward a large-scale open-source MmWave and terahertz experimental testbed," in *Proceedings of the 3rd ACM Workshop on Millimeter-Wave Networks and Sensing Systems*, ser. mmNets'19. Los Cabos, Mexico: Association for Computing Machinery, 2019, p. 27–32.
- [16] P. Ferrand, M. Amara, S. Valentin, and M. Guillaud, "Trends and challenges in wireless channel modeling for evolving radio access," *IEEE Communications Magazine*, vol. 54, no. 7, pp. 93–99, Jul. 2016.
- [17] M. Polese and M. Zorzi, "Impact of channel models on the end-to-end performance of mmWave cellular networks," in *IEEE 19th International Workshop on Signal Processing Advances in Wireless Communications (SPAWC)*, Jun. 2018.
- [18] T. Bai and R. W. Heath, "Coverage and rate analysis for millimeter-wave cellular networks," *IEEE Transactions on Wireless Communications*, vol. 14, no. 2, pp. 1100–1114, Feb. 2015.
- [19] J. Park, S.-L. Kim, and J. Zander, "Tractable resource management with uplink decoupled millimeter-wave overlay in ultra-dense cellular networks," *IEEE Transactions on Wireless Communications*, vol. 15, no. 6, pp. 4362–4379, Mar. 2016.
- [20] J. G. Andrews, T. Bai, M. N. Kulkarni, A. Alkhateeb, A. K. Gupta, and R. W. Heath, "Modeling and analyzing millimeter wave cellular systems," *IEEE Transactions on Communications*, vol. 65, no. 1, pp. 403–430, Jan. 2017.
- [21] I. A. Hemadeh, K. Satyanarayana, M. El-Hajjar, and L. Hanzo, "Millimeter-wave communications: Physical channel models, design considerations, antenna constructions, and link-budget," *IEEE Communications Surveys and Tutorials*, vol. 20, no. 2, pp. 870–913, Second Quarter 2018.
- [22] 3GPP, "Study on channel model for frequencies from 0.5 to 100 GHz," 3rd Generation Partnership Project (3GPP), Technical Report (TR) 38.901, Jun. 2018, version 15.0.0.
- [23] M. R. Akdeniz, Y. Liu, M. K. Samimi, S. Sun, S. Rangan, T. S. Rappaport, and E. Erkip, "Millimeter wave channel modeling and cellular capacity evaluation," *IEEE Journal on Selected Areas in Communications*, vol. 32, no. 6, pp. 1164–1179, Jun. 2014.
- [24] P. Testolina, M. Lecci, M. Polese, M. Giordani, and M. Zorzi, "Scalable and accurate modeling of the millimeter wave channel," in *International Conference on Computing, Networking and Communications (ICNC)*, Feb. 2020, pp. 969–974.
- [25] V. Degli-Esposti, F. Fuschini, E. M. Vitucci, M. Barbiroli, M. Zoli, L. Tian, X. Yin, D. A. Dupleich, R. Müller, C. Schneider, and R. S. Thomä, "Ray-tracing-based mm-Wave beamforming assessment," *IEEE Access*, vol. 2, pp. 1314–1325, 2014.
- [26] S. G. Larew, T. A. Thomas, M. Cudak, and A. Ghosh, "Air interface design and ray tracing study for 5G millimeter wave communications," in *IEEE Globecom Workshops (GC Wkshps)*, Dec. 2013, pp. 117–122.
- [27] C. Lai, R. Sun, C. Gentile, P. B. Papazian, J. Wang, and J. Senic, "Methodology for multipath-component tracking in millimeter-wave channel modeling," *IEEE Transactions on Antennas and Propagation*, vol. 67, no. 3, pp. 1826–1836, Mar. 2019.

- [28] T. R. Henderson, M. Lacage, G. F. Riley, C. Dowell, and J. Kopena, "Network simulations with the ns-3 simulator," vol. 14, no. 14, 2008, p. 527.
- [29] M. Mezzavilla, M. Zhang, M. Polese, R. Ford, S. Dutta, S. Rangan, and M. Zorzi, "End-to-end simulation of 5G mmWave networks," *IEEE Communications Surveys and Tutorials*, vol. 20, no. 3, pp. 2237–2263, Third Quarter 2018.
- [30] G. R. MacCartney and T. S. Rappaport, "Rural Macrocell Path Loss Models for Millimeter Wave Wireless Communications," *IEEE Journal on Selected Areas in Communications*, vol. 35, no. 7, pp. 1663–1677, Jul. 2017.
- [31] C. Gentile, P. B. Papazian, N. Golmie, K. A. Remley, P. Vouras, J. Senic, J. Wang, D. Caudill, C. Lai, R. Sun, and J. Chuang, "Millimeter-wave channel measurement and modeling: A NIST perspective," *IEEE Communications Magazine*, vol. 56, no. 12, pp. 30–37, Dec. 2018.
- [32] C. Wang, J. Bian, J. Sun, W. Zhang, and M. Zhang, "A Survey of 5G Channel Measurements and Models," *IEEE Communications Surveys and Tutorials*, vol. 20, no. 4, pp. 3142–3168, Fourth Quarter 2018.
- [33] T. S. Rappaport, Y. Xing, G. R. MacCartney, A. F. Molisch, E. Mellios, and J. Zhang, "Overview of millimeter wave communications for fifth-generation (5G) wireless networks – with a focus on propagation models," *IEEE Transactions on Antennas and Propagation*, vol. 65, no. 12, pp. 6213–6230, Dec. 2017.
- [34] M. Nakagami, "The m-distribution—a general formula of intensity distribution of rapid fading," in *Statistical Methods in Radio Wave Propagation*. Pergamon, 1960, pp. 3 – 36.
- [35] A. A. M. Saleh and R. Valenzuela, "A statistical model for indoor multipath propagation," *IEEE Journal on Selected Areas in Communications*, vol. 5, no. 2, pp. 128–137, Feb. 1987.
- [36] IST WINNER II, "D1.1.2 v1.2 WINNER II channel models," 2007.
- [37] M. Gapeyenko, V. Petrov, D. Moltchanov, S. Andreev, Y. Koucheryavy, M. Valkama, M. R. Akdeniz, and N. Himayat, "An Analytical Representation of the 3GPP 3D Channel Model Parameters for MmWave Bands," in *Proceedings of the 2nd ACM Workshop on Millimeter Wave Networks and Sensing Systems*, ser. mmNets '18. New Delhi, India: Association for Computing Machinery, 2018, p. 33–38. [Online]. Available: <https://doi.org/10.1145/3264492.3264498>
- [38] T. Zugno, M. Polese, N. Patriciello, B. Bojovic, S. Lagen, and M. Zorzi, "Implementation of A Spatial Channel Model for ns-3," 2020. [Online]. Available: <https://arxiv.org/abs/2002.09341>
- [39] J. Palacios, D. De Donno, and J. Widmer, "Tracking mm-Wave channel dynamics: Fast beam training strategies under mobility," in *IEEE Conference on Computer Communications (INFOCOM)*. IEEE, 2017.
- [40] W. Khawaja, O. Ozdemir, and I. Guvenc, "UAV Air-to-Ground Channel Characterization for mmWave Systems," in *IEEE 86th Vehicular Technology Conference (VTC-Fall)*, 2017, pp. 1–5.
- [41] C. Cordeiro *et al.*, "TGay evaluation methodology," 11-15/0866r4, IEEE Task Group ay (TGay), Tech. Rep., Jan. 2016, last update: May 2016.
- [42] F. Fuschini, E. M. Vitucci, M. Barbiroli, G. Falciasecca, and V. Degli-Esposti, "Ray tracing propagation modeling for future small-cell and indoor applications: A review of current techniques," *Radio Science*, vol. 50, no. 6, pp. 469–485, Jun. 2015.
- [43] Z. Yun and M. F. Iskander, "Ray tracing for radio propagation modeling: Principles and applications," *IEEE Access*, vol. 3, pp. 1089–1100, 2015.
- [44] J. Pascual-García, J. Molina-García-Pardo, M. Martínez-Inglés, J. Rodríguez, and N. Saurín-Serrano, "On the importance of diffuse scattering model parameterization in indoor wireless channels at mm-Wave frequencies," *IEEE Access*, vol. 4, pp. 688–701, 2016.
- [45] A. Maltsev *et al.*, "Channel models for IEEE 802.11ay," 11-15/1150r9, IEEE Task Group ay (TGay), Tech. Rep., Sep. 2015, last update: March 2017.

- [46] M. Lecci, M. Polese, C. Lai, J. Wang, C. Gentile, N. Golmie, and M. Zorzi, "Quasi-Deterministic Channel Model for mmWaves: Mathematical Formalization and Validation," submitted to IEEE Global Communications Conference (GLOBECOM), 2020. [Online]. Available: <https://arxiv.org/abs/2006.01235>
- [47] M. Polese, M. Giordani, M. Mezzavilla, S. Rangan, and M. Zorzi, "Improved handover through dual connectivity in 5G mmWave mobile networks," *IEEE Journal on Selected Areas in Communications*, vol. 35, no. 9, pp. 2069–2084, Sep. 2017.